HHS Public Access

Author manuscript

J Cardiovasc Transl Res. Author manuscript; available in PMC 2022 December 01.

Published in final edited form as:

J Cardiovasc Transl Res. 2021 December ; 14(6): 1131–1145. doi:10.1007/s12265-021-10130-y.

Computational Modeling Studies of the Roles of Left Ventricular Geometry, Afterload, and Muscle Contractility on Myocardial Strains in Heart Failure with Preserved Ejection Fraction

Sheikh Mohammad Shavik[1,2], **Samuel Wall**[3], **Joakim Sundnes**[3], **Julius M. Guccione**[4], **Partho Sengupta**[5], **Scott D. Solomon**[6], **Daniel Burkhoff**[7], **Lik Chuan Lee**[1]

[1]Department of Mechanical Engineering, Michigan State University, 428 S Shaw Lane, East Lansing, MI 48824, USA

[2]Department of Mechanical Engineering, Bangladesh University of Engineering and Technology, Dhaka 1000, Bangladesh

[3]Simula Research Laboratory, Oslo, Norway

[4]Department of Surgery, University of California, San Francisco, San Francisco, CA, USA

[5]Division of Cardiology, West Virginia Heart and Vascular Institute, Morgantown, WV, USA

[6]Brigham and Women's Hospital Division of Cardiovascular Medicine and Harvard Medical School, Boston, MA, USA

[7]Cardiovascular Research Foundation, New York, NY, USA

Abstract

Global longitudinal strain and circumferential strain are found to be reduced in HFpEF, which some have interpreted that the global left ventricular (LV) contractility is impaired. This finding is, however, contradicted by a preserved ejection fraction (EF) and confounded by changes in LV geometry and afterload resistance that may also affect the global strains. To reconcile these issues, we used a validated computational framework consisting of a finite element LV model to isolate the effects of HFpEF features in affecting systolic function metrics. Simulations were performed to quantify the effects on myocardial strains due to changes in LV geometry, active tension developed by the tissue, and afterload. We found that only a reduction in myocardial contractility and an increase in afterload can simultaneously reproduce the blood pressures, EF and strains measured in HFpEF patients. This finding suggests that it is likely that the myocardial contractility is reduced in HFpEF patients.

Keywords

HFpEF; Global longitudinal strain; Myocardial contractility; Finite element modeling

✉Lik Chuan Lee, lclee@egr.msu.edu.

Conflict of Interest All the authors declare that they have no conflict of interest.

Ethical Approval This article does not contain any studies with human participants or animals performed by any of the authors.

Introduction

Heart failure with preserved ejection fraction (HFpEF) is a syndrome accounting for about one-half of all chronic heart failure (HF) patients [1, 2]. The incidence and prevalence of HFpEF are increasing at a rate of about 1%/year [2, 3], with mortality rates comparable to HF with reduced ejection fraction (HFrEF) [2, 4, 5]. Compared to HFrEF, patients diagnosed with HFpEF are older and have a higher prevalence rate of hypertension [2]. While new therapies have been proposed [6–10], no proven treatment option currently exists for HFpEF patients [11, 12].

Because of the presence of many pathological features impairing LV filling [13] (e.g., slow LV relaxation [14], cardiomyocyte stiffening [14], concentric hypertrophy [15]), diastolic dysfunction was initially believed to be the sole mechanism underlying HFpEF, which was previously referred to as diastolic HF [3, 16]. Mounting evidence, however, has suggested that myocardial contractility in HFpEF patients may also be impaired, thus calling into question the original notion that systolic myocardial function is preserved in this syndrome [17–20]. However, seemingly contradictory observations have been challenging to reconcile and are unable to resolve the question of myocardial contractility in HFpEF. On the one hand, studies have shown that LV ejection fraction (EF) is normal or increased in HFpEF (suggesting preserved or increased global *ventricular* contractility) [21, 22]. On the other hand, these hearts exhibit decreased global longitudinal strain (E_{ll}) and circumferential strain (E_{cc}) [17] suggesting decreased *myocardial* contractility.

These seemingly conflicting observations (preserved chamber contractility but decreased myocardial deformation) are difficult to resolve purely through basic or clinical experimental studies. This difficulty arises because of the differing influences of increased vascular resistance (afterload), altered LV geometry and increased LV mass (all encountered in HFpEF patients) on longitudinal strain, which potentially confound the link between longitudinal and circumferential strains, as well as myocardial contractility.

Computational modeling has the inherent advantage to isolate factors affecting LV function and motion in HFpEF patients so as to clarify their individual role(s) and contribution(s). There are, however, only a few prior studies that have explored the use of computational modeling to understand ventricular mechanics in HFpEF [23–26]. However, the seemingly conflicting observations and multiple confounding factors as described above, to the best of our knowledge, have not been resolved in any of those studies.

Accordingly, the purpose of this study was to determine whether decreased longitudinal and circumferential strains encountered in HFpEF is truly a reflection of decreased myocardial contractility or is this simply due to the combined effects of altered LV mass, geometry and/or afterload resistance. To do so, we employed a computational modeling framework whose parameters were adjusted to replicate key characteristics of heart and vascular properties in HFpEF. Resolution of this question is important because of its implication for advancing understanding of HFpEF, which may also help guide the development of new therapies.

Methods

Computational Modeling Framework

A coupled left ventricle (LV)–closed-loop circulatory computational modeling framework (Fig. 1a) was used to simulate the hemodynamics and ventricular mechanics of HFpEF [27, 28]. In this framework, the LV was modeled using the finite element (FE) method with a realistic 3D ventricular geometry to simulate a beating LV. The mechanical behavior of the LV was described by an active stress formulation.

In this formulation, the active force developed along the local myofiber direction was calculated using a modified time-varying elastance model that takes into account length-dependency of the muscle fiber [29], whereas the passive mechanical behavior was described using a Fung-type transversely isotropic hyperelastic constitutive model [30]. The LV FE model was coupled to closed-loop lumped parameter circulatory model describing the systemic circulation. The circuit consists of proximal and distal arterial and venous compliances ($C_{a,\,p}$, $C_{a,\,d}$ and C_{ven}) and resistances ($R_{a,\,p}$, $R_{a,\,d}$ and R_{ven}), mitral and aortic valves (with resistances R_{ao} and R_{mv}) and left atrium (LA). Contraction of the LA was described using a time-varying elastance function. Details of the governing equations for the computational modeling framework are given in Appendix A. These governing equations were solved using the finite element method with the open-source library FEniCS [31]. The number of quadratic elements used is 1049, which has been shown is sufficient for convergence [27].

Left Ventricular Geometry and Boundary Conditions

An idealized prolate ellipsoid was used to model the LV typical of that found in normal humans and HFpEF patients. Clinical studies have shown that the LV in HFpEF patients has both increased wall thickness to cavity diameter (internal dimension) ratio and apex-to-base length compared to healthy subjects [32–34]. Some studies, however, have also found that the LV cavity diameter was either not significantly different or slightly decreased (but both with thicker ventricular wall) in HFpEF patients [35, 36]. To reflect the wide spectrum of LV geometry found in HFpEF patients, we applied 2 different LV geometries in the modeling framework to simulate HFpEF, namely, one with a smaller LV cavity (HFpEF I) and one with a slightly dilated LV cavity (HFpEF II) with respect to a normal LV geometry. Both HFpEF geometries had a thicker wall and increased mass compared to that in the *normal* case (Fig. 1b).

The same boundary conditions as in previous computational models [28, 37, 38] were applied in all simulations for the LV model. For the *normal* case, the myofiber direction (helix angle) was varied transmurally across the LV wall with a linear variation from 60° at the endocardium to −60° at the epicardium based on a previous experimental measurement [39]. The relaxation time constant τ was set at 25ms, which is within the normal range [14] (Eq. (14) in Appendix).

Analysis of Strains

Global longitudinal strain E_{ll} and circumferential strain E_{cc} were calculated using the method described by Shavik *et al* [27] with end-diastole serving as the reference configuration. Myofiber stretch in the longitudinal and circumferential directions, denoted respectively by $\boldsymbol{e_l}$ and $\boldsymbol{e_c}$, were first computed by

$$\lambda_i = \sqrt{\mathbf{e}_i} \cdot \mathbf{C} \cdot \mathbf{e}_i \,. \tag{1}$$

In the above equation, $\boldsymbol{C} = \boldsymbol{F}^{\boldsymbol{T}}\boldsymbol{F}$ is the right Cauchy–Green deformation tensor, $\boldsymbol{F}$ is the deformation gradient tensor, and $\boldsymbol{e_i}$ with $i \in (l, c)$ are the unit vectors in the longitudinal l and circumferential c directions, respectively. The circumferential direction $\boldsymbol{e_c}$ was defined to be orthogonal to the radial direction and the apex to base direction. The longitudinal direction $\boldsymbol{e_l}$ was then defined to be orthogonal to both radial direction and $\boldsymbol{e_c}$. The strain was calculated using [27]

$$\varepsilon_{ii} = \frac{1}{2}\left(1 - \frac{1}{\lambda_i^2}\right) \times 100\,\% \,. \tag{2}$$

Simulation Cases

A *normal* case was first simulated so that the LV geometrical features at end-diastole and end-systole and hemodynamics, as well as global E_{cc} and E_{ll} (waveforms and peak values), were close (within 1 standard deviation) to the values reported in control subjects in clinical HFpEF studies [17, 32, 40]. Having established the parameters for the *normal* case, we then applied them to the 2 HFpEF geometries in cases *G1* and *G2*. Preload was increased in these 2 cases by adjusting the resting venous volume (V_{ven0}) and the passive stiffness was increased (in HFpEF I geometry) so that LV end-diastolic pressure (EDP) is in the range of 18–25 mmHg found in HFpEF patients [36, 41]. The relaxation time constant $\boldsymbol{\tau}$ was set at 50ms (cf. 25ms in the *normal* case) to reflect the larger values found in HFpEF patients [42].

Using *G1* and *G2* as the reference cases, we then simulated a number of cases to isolate the effects of (1) active tension developed by the tissue (i.e., myocardial contractility) and (2) ventricular afterload as indexed by arterial resistance, which are factors deemed to affect E_{ll} in HFpEF. The effect of afterload is considered here because a majority of HFpEF patients have hypertension [43]. Active tension and afterload were changed, respectively, by scaling the active stress (T_{ref}) and the peripheral resistance ($R_{a,\,d}$) so that E_{ll} fell within the range of values measured in the clinical study [17]. Based on the insights derived from these cases, we then systematically modified the parameter values (that reflect a combination of these factors) to arrive at a combination that simultaneously fit all the conditions (volume, EF, strains, blood pressures) encountered in HFpEF patients [17]. As explained later, the myofiber direction (helix angle) also had to be slightly adjusted to simulate the HFpEF conditions. Heart rate was set constant at 75 bpm for all simulations, consistent with data reported in prior studies measured under resting conditions [17, 32]. All simulation cases are summarized with labels in Table 1 and the model parameters are given in Tables 3, 4, 5 and 6 in the Appendix.

Results

Validation of *Normal* Case

Model predictions for the *normal* case are in agreement with clinical measurements (Fig. 2). Specifically, the LV end-diastolic volume (EDV) (109ml), ejection fraction (EF) (60%) and LV wall thickness at end-diastole (EDWT) (0.8cm) are all within the normal range found in healthy humans [34, 44]. Diastolic blood pressure (DBP) (77 mmHg), systolic blood pressure (SBP) (132 mmHg), peak absolute E_{cc} (29%), and E_{ll} (21%) are all close to the values found in the clinical measurements of the control in a study on HFpEF patients (EF: 61 ± 3%; DBP: 74 (68, 84) mmHg; SBP: 130 (118, 138) mmHg; E_{cc}: 27.1 ± 3.1%; E_{ll}: 20 ± 2.1%) [17]. The E_{cc} and E_{ll} waveforms are also in agreement with echo measurements of healthy humans [45–47] (Fig. 2c and d). Internal diameter and EDWT are also in agreement with those measured in normal humans (Table 2).

Effects of Changes in Geometry, Passive Stiffness, and Preload

Changing the LV geometry and elevation of the preload in cases *G1* and *G2* produced a larger LV wall thickness at ED (~1cm) and normal EF (~65%), which are within the measured range in HFpEF patients [34, 44] (Table 2, Fig. 3). Peak (absolute) E_{cc} was reduced to 24% in *G1* and 20% in *G2*, which are also within the range measured in HFpEF patients [17]. Peak E_{ll}, however, was relatively insensitive to these changes and was only slightly reduced (18.2% in *G1* and 20% in *G2*), with values well above the measured values in HFpEF patients (~14.6%) [17]. We note that *G2* (larger LV EDV) produced a higher SBP and DBP that were above the range measured in HFpEF patients. Conversely, SBP and DBP did not change substantially in *G1* (smaller LV EDV). The changes associated with *G1* and *G2* also produced a larger EF compared to normal.

Effects of Afterload

Increasing the afterload led to a decrease in peak E_{cc} and E_{ll} (Fig. 4). For both HFpEF geometries, the decrease in peak E_{cc} was substantially more. An increase in SBP by 32 mmHg (from 129 in *G1* to 161 mmHg in *G1-A2*) in HFpEF I geometry produced a decrease in peak E_{cc} by 4.7% (from 24 to 19.3%). Similarly, an increase in SBP by 47 mmHg (from 155 in *G2* to 202 mmHg in *G2-A2*) in HFpEF II geometry produced a decrease in peak E_{cc} by 8.1% (from 20 to 11.9%). Corresponding to these increments in SBP, E_{ll} was only reduced by 1.2% (from 18.2 to 17%) in HFpEF I and 2.5% (from 20 to 17.5%) in HFpEF II. Ejection fraction was reduced with increasing afterload, but remained above 50% for all these cases except for *G2-A2* (with the highest afterload). We note while E_{ll} fell within the clinical measurements of HFpEF patients [17] for these cases associated with increased afterload, their SBP and/or DBP were all outside the clinical measurements.

Effects of Myocardial Contractility

Reducing myocardial contractility uniformly across the myocardial wall produced a decrease in SBP, DBP, peak E_{cc} and E_{ll} in both HFpEF geometries (Fig. 5). Decreasing myocardial contractility by 60% in HFpEF I and 46% in HFpEF II produced a substantial reduction in peak E_{cc} by 12.7% (from 24 to 11.3%) and 8.9% (from 20 to 11.1%), respectively.

Similar to afterload, peak E_{ll} is less sensitive to myocardial contractility than peak E_{cc}. The same decrement in myocardial contractility produced only a 2.2% decrease in E_{ll} (from 18.2 to 16.0%) in HFpEF I geometry and 2.1% decrease in E_{ll} (from 20 to 17.9%) in HFpEF II geometry. These reductions were accompanied by a substantial reduction in SBP from 129 to 94 mmHg in HFpEF I and 155 to 121 mmHg in HFpEF II. Ejection fraction was decreased with myocardial contractility, and was below 50% in *G1-C2* and *G2-C2* associated with the largest reduction in myocardial contractility.

Effects of Simultaneous Changes of Both Afterload and Myocardial Contractility

As described thus far, none of the simulation cases associated with isolated changes in geometry, preload and passive stiffness, or these in combination with either an increase in afterload or a decrease in myocardial contractility, simultaneously reproduced the blood pressure, LV EF and strain measurements reported in HFpEF patients [17]. Accordingly, based on the results of these simulations, we varied the parameters to simultaneously reproduce the clinical measurements of HFpEF patients. For HFpEF I geometry, peak E_{ll} was just within the range of measurements in *G1-A1*, but its DBP was above the measured values (Fig. 6a). Further increases or decreases in afterload would therefore cause DBP and E_{ll} to be out of range, respectively. The same argument also applies for myocardial contractility, where further increases or decreases in *G1-C1* will cause E_{ll} and SBP/DBP to be out of range (Fig. 5a). As such, only a combination of increased afterload and reduced myocardial contractility can reproduce all the HFpEF measurements (*G1-C-A*). This combination, however, just replicates all the measurements. Inclusion of a small change of myofiber angle by 5° (i.e., linear variation from 55° at endocardium to −55° at the epicardium) (*G1-C-A-55*) provided a significantly better fit to peak E_{ll} and E_{cc} in addition to all the other measurements (Fig. 6a).

For HFpEF II geometry, we note that changing the LV geometry to *G2* already produces SBP and DBP that are higher than the clinical measurements with E_{ll} still above the measured range. Thus, it is impossible to concurrently fit the clinical measurements of SBP, DBP, and E_{ll} by purely adjusting the afterload. Similarly, we note that *G2-C1*'s EF, SBP, and DBP are all within the clinical range but E_{cc} and E_{ll} are below and above the range of measured values, respectively (Fig. 5b). While further decrease in myocardial contractility or increase in afterload reduced E_{ll} to within the clinical range, it caused E_{cc} to be much lower than the clinical range. Given this constraint, we find that the only alternative to simultaneously fit E_{cc} and E_{ll} (as well as other conditions) is to slightly reduce the myofiber angle (by 5° and 10°) and make the muscle fiber more circumferential (Fig. 6b).

Discussion

We used a computational modeling framework to determine if reduced longitudinal strain observed in HFpEF patients was due to reduced myocardial contractility, an increase in afterload resistance and/or the accompanying altered geometry. Starting from a *normal* case that was validated against measurements of LV geometry (EDV, EDWT, mass), function (EF, E_{cc}, E_{ll}, τ) and hemodynamics (DBP, SBP, EDP) in healthy humans (including the controls of several HFpEF studies [17, 32, 34]), we first show that a change in LV geometry, passive

stiffness and preload to those found in HFpEF patients, without any other changes, decreases peak E_{cc} and E_{ll} (Fig. 4). While the decrease in E_{cc} is within the clinical measurements, the decrease in E_{ll} is, however, moderate (~2 to 3%, absolute) and is less than half of that measured in HFpEF patients [17]. This result is irrespective of the 2 HFpEF geometries (both with thicker LV wall and increased mass) that we considered here (i.e., HFpEF I with smaller LV cavity and HFpEF II with a slightly larger LV cavity compared to normal). Based on this, *we conclude that the decrease in E_{ll} (along with other changes) found in HFpEF patients cannot be explained solely by a mere change in LV geometry, pre-load, and passive stiffness*.

Next, we tested the hypothesis that the reduction in E_{ll} associated with HFpEF can be explained by either an increase in afterload (given that hypertension is present in 60% of HFpEF patients in the clinical study [17] and has a prevalence of 55–86% in HFpEF patients [43]) or a decrease in myocardial contractility. By superimposing these changes with a change in LV geometry, preload and/or passive stiffness in the simulations, we found that these changes, when imposed in isolation, could not simultaneously reproduce reported values of SBP, DBP, EF, E_{cc}, and E_{ll} in HFpEF patients. In both HFpEF geometries considered here, increasing afterload reduced E_{cc} and E_{ll} to the level found in HFpEF patients but produce SBPs and DBPs that are well above the measurements, and unphysiologically high (> 180 mmHg) for a slightly dilated HFpEF geometry (Fig. 4). Similarly, reducing myocardial contractility in the LV produced E_{cc} and E_{ll} that agreed with the measurements, but caused SBPs and DBPs below the measured values (Fig. 5). As such, *we conclude that the reduction in E_{ll} in HFpEF cannot be produced by isolated changes in afterload or myocardial contractility*.

Finally, we investigated the combined changes of myocardial contractility, afterload and myofiber angle changes that can simultaneously produce the conditions in SBP, DBP, EF, E_{ll}, and E_{cc} all with magnitudes similar to those found in HFpEF patients [17]. As explained in the “Effects of Simultaneous Changes of Both Afterload and Myocardial Contractility” section, we found that a combination of reduced myocardial contractility (16%) and increase in afterload (20%) marginally reproduced all the above changes for HFpEF I geometry (smaller LV). A slight reduction in myofiber angle of 5° (i.e., more circumferential myofibers across the ventricular wall) provided a better fit to all target parameters. For HFpEF II geometry (dilated LV), a combination of reduced myocardial contractility (30%) and slight reduction in myofiber angle (5 to 10°) can reproduce all the conditions in HFpEF patients. We therefore conclude that *the reduction in E_{ll} in HFpEF can only be explained by a reduction in myocardial contractility and may be accompanied a small degree of myofiber reorientation*.

Due in part to the heterogeneity of clinical characteristics encountered in HFpEF patients, the pathophysiology of HFpEF is likely to be multifactorial [11, 48]. It is essentially impossible to unravel the relative contributions of these multiple factors to changes in longitudinal strain purely from clinical observations or experiments. Computational modeling, on the other hand, is an important tool that can serve this purpose. While there are some computational modeling studies of HFpEF [23, 24, 49], the existing studies, to the best of our knowledge, have not comprehensively assessed the contributions of changes in

afterload, tissue active tension and geometry to abnormalities in both hemodynamics (SBP and DBP) and functional indices (E_{ll} and E_{cc}) found in HFpEF patients.

The key model prediction that the decrease in E_{ll} in HFpEF patients must be accompanied by a reduction in myocardial contractility compares favorably with measurements of myocyte active tension from biopsy samples of hypertensive patients exhibiting diastolic dysfunction and concentric LV remodeling [50, 51]. Specifically in patients undergoing coronary bypass grafting, maximum developed isometric tension of isolated myocytes was found to be about 50% lower in those with hypertension, concentric remodeling but with normal EF compared to those without hypertension (10.67 ± 1.38 vs. 20.64 ± 3.29 mN/mm^2) [50]; this is regardless of whether the patients had heart failure or not. Similarly, myocyte isometric tension was also found to be lower (though not statistically significant) in patients who had hypertension and diastolic heart failure compared to the recipients of heart transplants (20.3 ± 7.5 vs. 24.2 ± 12.4 kN/m^2) [51]. This key model prediction is also largely consistent with previous modeling studies, with one suggesting that the active tension of myocytes is reduced at the subendocardial region but is increased at the subepicardial region in the LV of HFpEF patients [23], and the other suggesting the systolic contractile force is reduced in HFpEF due to abnormal calcium homeostasis [25]. We note that some clinical measurements, however, showed that epicardial (as well as endocardial) E_{ll} is significantly reduced in HFpEF patients (cf. normal) by about 4% [52], 2.4% [53] and 5% (mid LV) [54]. These results suggest that contractility is likely to be reduced also in the epicardial region because an increase in contractility in that region would have locally produced an increase in peak myofiber strain [23].

Our simulations also suggest that the reduction in E_{ll} in HFpEF patients may also be driven by a slight reorientation of the myofiber circumferentially. This result is consistent with a recent study that uses diffusion tensor magnetic resonance imaging to characterize the myocardial microstructure in patients with cardiac amyloidosis and exhibiting concentric hypertrophy with preserved EF [55]. The study found that these patients had reduced longitudinal orientation of the myofiber in the epicardial and endocardial layer, and these microstructural changes are strongly correlated with a reduction in global longitudinal strain. We also note that while a few histological studies have reported no change in the myofiber orientation [56] associated with concentric LV remodeling, the small change of 5 to 10° predicted by the model may not be detectable given that the standard deviation of typical histological studies is ~10° [57].

Our findings support the previously proposed interpretation that a reduction in E_{ll} in HFpEF patients relates, in large part, to a reduction in myocardial contractility. While this conclusion does not *a priori* imply that inotropes are a potential treatment for HFpEF, it does contribute to the growing body of evidence documenting similarities of myocardial pathologies across the range of EFs [58]. Indeed, many of the abnormalities leading to systolic dysfunction also contribute to impaired diastolic function. For example, abnormalities of calcium metabolism by the sarcoplasmic reticulum contribute to both decreased contractility and decreased rate of relaxation [59]. Accordingly, based on such suppositions and detailed analyses, it has been suggested that despite failed studies, neurohormonal blockers may provide benefit at least in some segment of the chronic HFpEF

population [58]. Furthermore, the prior clinical studies on which our analysis is based only examined LV function at rest; whether or not impaired resting systolic function at rest is also associated with impaired contractile reserve has not been assessed. Such an abnormality could contribute to exercise intolerance that is characteristic of HFpEF. The current findings highlight the need to determine whether and the degree to which reduced myocardial contractility contributes to symptoms or prognosis in HFpEF.

Model Limitations

The current findings need to be interpreted within the context of potential limitations. First, we have assumed the LV geometry to be an idealized truncated ellipsoid (for simplicity), and consequently, did not consider any asymmetrical geometrical differences (e.g., focal hypertrophy of the interventricular septum [60]), patient-specific variability (due to multifactorial nature of the disease) or possible effects of the right ventricle. Patient-specific geometrical (as well as hemodynamics and functional) variability can be considered in future studies by repeating the analysis on a sample of patient-specific data (with sufficient statistical power), which is substantially more involved and complex. Second, we do not consider regional or transmural changes in myocardial contractility in this study. Due to the transmural differences in metabolism [61] and perfusion [62], changes in myocardial contractility may be different across the LV wall as suggested in one study [23]. Future study will investigate the effects of any transmural changes in myocardial contractility in HFpEF. Third, we have confined our study to longitudinal and circumferential strains, and did not investigate ventricular torsion that has been found to be reduced in HFpEF [63]. Fourth, we have only considered ventricular properties under resting conditions as the clinical measurements were performed under those conditions. However, symptoms and hemodynamic abnormalities of many HFpEF patients are manifested and exaggerated even during mild exertion. Whether this reflects an alteration of intrinsic ventricular properties or a more complex interplay between peripheral and ventricular properties is currently unknown and not addressed in the present analysis. Fifth, we did not consider the effects of left atrial (LA) dysfunction, which may be present (e.g., lower LA peak strain) given that the LA is exposed to an elevated LV filling pressure in HFpEF [64]. Finally, we have focused largely on modeling features from the data acquired in a number of clinical studies [17, 19, 32] that do not distinguish between the time course over which HFpEF has developed. As such, the findings here reproduce the observations in a cross-section of HFpEF patients, and do not correspond to any specific etiology and/or time point during disease progression. Given that the clinical data that this study was based on show a reduction in both circumferential and longitudinal strains, the findings here may correspond to a more advanced phenotype of HFpEF as suggested in a study [65]. Future studies with longitudinal data will be able to help characterize the time course of the alteration of ventricular properties in HFpEF patients.

Summary and Conclusion

Based on a validated FE computational model, we replicated key aspects of ventricular geometry, chamber size, blood pressure, LV EF, and circumferential and longitudinal strain reported in HFpEF patients. Optimal matching of model prediction to all these features was

achieved only through simultaneous reduction of myocardial contractility with a moderate reduction in the myofiber helix angle and an increase in afterload. Thus, we conclude that the reduction of longitudinal strain reflects a reduction of myocardial contractility in HFpEF and is not simply a reflection of increased afterload or altered geometry. In view of the fact that reduced longitudinal strain has been associated with worse survival in HFpEF patients [66], the current results provide an important clarification of the mechanisms by which strain is reduced.

Funding

This study was funded by the American Heart Association (AHA) grant 17SDG33370110 and the National Institutes of Health (NIH) R01 HL134841.

Appendix

Closed Loop Systemic Circulatory Model

The LV FE model was coupled to a closed loop lumped-parameter circulatory model that describes the systemic circulation (Fig. 1), which is similar to our previous work [27]. The modeling framework consists of five compartments of the systemic circulation namely, LV, LA, proximal artery, distal artery, and vein. The total mass of blood needs to be conserved in the circulatory model, which requires that the rate of volume change in each storage compartment of the circulatory system to the inflow and outflow rates by the following relations,

$$\frac{dV_{LA}(t)}{dt} = q_{ven}(t) - q_{mv}(t), \tag{1a}$$

$$\frac{dV_{LV}(t)}{dt} = q_{mv}(t) - q_{ao}(t), \tag{1b}$$

$$\frac{dV_{a,\,p}(t)}{dt} = q_{ao}(t) - q_{a,\,p}(t), \tag{1c}$$

$$\frac{dV_{a,\,d}(t)}{dt} = q_{a,\,p}(t) - q_{a,\,d}(t), \tag{1d}$$

$$\frac{dV_{ven}(t)}{dt} = q_{a,\,d}(t) - q_{ven}(t), \tag{1e}$$

where V_{LA}, V_{LV}, $V_{a,\,p}$, $V_{a,\,d}$, and V_{ven} are volumes of LV, LA, proximal artery, distal artery, and vein, respectively, and q_{ven}, q_{mv}, q_{ao}, $q_{a,\,p}$, and $q_{a,\,d}$ are flow rates at different segments. Flowrate at different segments of the circulatory model depends on their resistance to flow (R_{ao}, $R_{a,\,p}$, $R_{a,\,d}$, R_{ven}, and R_{mv}) and the pressure difference between the connecting storage compartments (i.e., pressure gradient). The flow rates are given by

$$q_{ao}(t) = \begin{cases} \dfrac{P_{LV}(t) - P_{a,p}(t)}{R_{ao}} & when, P_{LV}(t) \geq P_{a,p}(t) \\ 0 & when, P_{LV}(t) < P_{a,p}(t) \end{cases}, \tag{2a}$$

$$q_{a,p}(t) = \frac{P_{a,p}(t) - P_{a,d}(t)}{R_{a,p}}, \tag{2b}$$

$$q_{a,d}(t) = \frac{P_{a,d}(t) - P_{ven}(t)}{R_{a,d}}, \tag{2c}$$

$$q_{ven}(t) = \frac{P_{ven}(t) - P_{LA}(t)}{R_{ven}}, \tag{2d}$$

$$q_{mv}(t) = \begin{cases} \dfrac{P_{LA}(t) - P_{LV}(t)}{R_{mv}} & when, P_{LA}(t) \geq P_{LV}(t) \\ 0 & when, P_{LA}(t) < P_{LV}(t) \end{cases}. \tag{2e}$$

Pressure in each storage compartment is a function of its volume. A simplified pressure–volume relationship

$$P_{a,p}(t) = \frac{V_{a,p}(t) - V_{ap,0}}{C_{a,p}}, \tag{3a}$$

$$P_{a,d}(t) = \frac{V_{a,d}(t) - V_{ad,0}}{C_{a,d}}, \tag{3b}$$

$$P_{ven}(t) = \frac{V_{ven}(t) - V_{ven,0}}{C_{ven}}, \tag{3c}$$

was prescribed for the proximal artery, distal artery, and veins, where $V_{ap,0}$, $V_{ad,0}$, and $V_{ven,0}$ are constant resting volumes of the proximal artery, distal artery, and veins. $C_{a,p}$, $C_{a,d}$, and C_{ven} are the total compliance of the proximal artery, distal artery, and venous system. On the other hand, pressure in the left atrium $P_{LA}(t)$ was prescribed to be a function of its volume $V_{LA}(t)$ by the following equations that describe its contraction using a time-varying elastance function [67]

$$P_{LA}(t) = e(t)P_{es,LA}(V_{LA}(\mathrm{t})) + (1 - e(t))P_{ed,LA}(V_{\mathrm{LA}}(\mathrm{t})), \tag{4}$$

where

$$P_{es,LA}(V_{LA}(\mathrm{t})) = E_{es,LA}(V_{LA}(\mathrm{t}) - V_{0,LA}), \tag{5a}$$

$$P_{ed,\,LA}(V_{LA}(\mathrm{t})) = A_{LA}\left(e^{B_{LA}\left(V_{LA}(\mathrm{t}) - V_{0,\,LA}\right)} - 1\right), \tag{5b}$$

and,

$$e(t) = \begin{cases} \frac{1}{2}\left(\sin\left[\left(\frac{\pi}{t_{max}}\right)t - \frac{\pi}{2}\right] + 1\right); & 0 < t \le 3/2\ t_{max} \\ \frac{1}{2}e^{-(t\ -\ 3/2t_{max})/\tau_{LA}}; & t > 3/2\ t_{max} \end{cases}. \tag{5c}$$

In Eqs. (5a–b), $E_{es,\,LA}$ is the end-systolic elastance of the left atrium, $V_{0,\,LA}$ is the volume axis intercept of the end-systolic pressure–volume relationship (ESPVR), and both A_{LA} and B_{LA} are parameters of the end-diastolic pressure–volume relationship (EDPVR) of the left atrium. The driving function $e(t)$ is given in Eq. (5c) in which t_{max} is the point of maximal chamber elastance and τ is the time constant of relaxation. The values of $E_{es,\,LA}$, $V_{0,\,LA}$, A_{LA}, B_{LA}, t_{max}, and τ_{LA} are listed in Table 3.

Finally, pressure in the LV depends on its corresponding volume through nonclosed form function

$$P_{LV}(t) = f^{LV}(V_{LV}(t)), \tag{6}$$

The functional relationship between pressure and volume in the LV was obtained using the FE method as described in the next section. Parameter values associated with the closed loop circulatory model are tabulated in Table 4.

Table 3

Fixed parameters of LA time varying elastance model for all cases

Parameter	Unit	Values
End-systolic elastance, $E_{es,\,LA}$	Pa/ml	60
Volume axis intercept, $V_{0,\,LA}$	ml	10
Scaling factor for EDPVR, A_{LA}	Pa	2.67
Exponent for EDPVR, B_{LA}	ml^{-1}	0.019
Time to end-systole, T_{max}	msec	120
Time constant of relaxation, τ	msec	25

Table 4

Fixed parameter values of the circulatory model for all simulation cases

Parameter	Unit	Values
Aortic valve resistance, R_{ao}	Pa ms ml^{-1}	500
Proximal aorta resistance, $R_{a,\,p}$	Pa ms ml^{-1}	18,000
Venous resistance, R_{ven}	Pa ms ml^{-1}	100

Parameter	Unit	Values
Mitral valve resistance, R_{mv}	Pa ms ml^{-1}	200
Proximal aorta compliance, $C_{a,p}$	ml Pa	0.0032
Distal aorta compliance, $C_{a,d}$	ml Pa	0.033
Venous compliance, C_{ven}	ml Pa	0.28
Resting volume for proximal aorta, $V_{ap,0}$	ml	360
Resting volume for distal aorta, $V_{ad,0}$	ml	40

Finite Element Formulation of the LV

The weak form associated with finite element formulation of the LV was derived based on the minimization of the following Lagrangian functional [28, 37],

$$\mathscr{L}(\boldsymbol{u}, p, P_{\text{cav}}, \boldsymbol{c}_1, \boldsymbol{c}_2) = \int_{\Omega_0} W(\boldsymbol{u}) dV - \int_{\Omega_0} p(J-1) dV - P_{\text{cav}}(V_{\text{cav}}(\boldsymbol{u}) - V) - \boldsymbol{c}_1 \cdot \int_{\Omega_0} \boldsymbol{u}\, dV - \boldsymbol{c}_2 \cdot \int_{\Omega_0} \boldsymbol{X} \times \boldsymbol{u}\, dV, \tag{7}$$

where, $\boldsymbol{u}$ is the displacement field, P_{cav} is the Lagrange multiplier to constrain the LV cavity volume $V_{\text{cav}}(\boldsymbol{u})$ to a prescribed value V [68], p is a Lagrange multiplier to enforce incompressibility of the tissue (i.e., Jacobian of the deformation gradient tensor $J = 1$), and both $\boldsymbol{c}_1$ and $\boldsymbol{c}_2$ are Lagrange multipliers to constrain rigid body translation (i.e., zero mean translation) and rotation (i.e., zero mean rotation) [[69]]. The LV cavity volume V_{cav} is a function of the displacement $\boldsymbol{u}$ and is defined by

$$V_{\text{cav}}(\boldsymbol{u}) = \int_{\Omega_{inner}} dv = -\frac{1}{3} \int_{\Gamma_{inner}} \boldsymbol{x} \,.\, \boldsymbol{n}\, da, \tag{8}$$

where Ω_{inner} is the volume enclosed by the inner surface Γ_{inner} and the basal surface at $z = 0$, and $\boldsymbol{n}$ is the outward unit normal vector.

Pressure–volume relationship of the LV required in the lumped parameter circulatory model (i.e., Eqs. (6)) was defined by the solution obtained from minimizing the functional [27]. Taking the first variation of the functional in Eq. (7) leads to the following expression:

$$\begin{aligned} \delta\mathscr{L}(\boldsymbol{u}, p, P_{\text{cav}}, \boldsymbol{c}_1, \boldsymbol{c}_2) = & \int_{\Omega_0} \left(\boldsymbol{P} - p\boldsymbol{F}^{-T}\right) \\ & : \nabla \delta\boldsymbol{u}\, dV - \int_{\Omega_0} \delta p(J-1) dV - P_{\text{cav}} \int_{\Omega_0} cof(\boldsymbol{F}) \\ & : \nabla \delta\boldsymbol{u}\, dV - \delta P_{\text{cav}}(V_{\text{cav}}(\boldsymbol{u}) - V) - \delta\boldsymbol{c}_1 \cdot \int_{\Omega_0} \boldsymbol{u}\, dV - \delta\boldsymbol{c}_2 \cdot \int_{\Omega_0} \boldsymbol{X} \\ & \times \boldsymbol{u}\, dV - \boldsymbol{c}_1 \cdot \int_{\Omega_0} \delta\boldsymbol{u}\, dV - \boldsymbol{c}_2 \cdot \int_{\Omega_0} \boldsymbol{X} \times \delta\boldsymbol{u}\, dV\,. \end{aligned} \tag{9}$$

In Eq. (9), $\boldsymbol{P}$ is the first Piola Kirchhoff stress tensor, $\boldsymbol{F}$ is the deformation gradient tensor, $\delta\boldsymbol{u}$, δp, δP_{cav}, $\delta\boldsymbol{c}_1$, $\delta\boldsymbol{c}_2$ are the variation of the displacement field, Lagrange multipliers for enforcing incompressibility and volume constraint, zero mean translation and rotation, respectively. The Euler-Lagrange problem then becomes finding $\boldsymbol{u} \in H^1(\Omega_0)$, $p \in L^2(\Omega_0)$, $P_{\text{cav}} \in \mathbb{R}$, $\boldsymbol{c}_1 \in \mathbb{R}^3$, $\boldsymbol{c}_2 \in \mathbb{R}^3$ that satisfies

$$\delta\mathscr{L}(\boldsymbol{u}, p, P_{\text{cav}}, \boldsymbol{c}_1, \boldsymbol{c}_2) = 0 \tag{10}$$

and $\boldsymbol{u}(x, y, 0).\boldsymbol{n}|_{base} = 0$ (for constraining the basal deformation to be in-plane) $\forall\, \delta\boldsymbol{u}(\Omega_0)$, $\delta p \in L^2(\Omega_0)$, $\delta P_{\text{cav}} \in \mathbb{R}$, $\delta\boldsymbol{c}_1 \in \mathbb{R}^3$, $\delta\boldsymbol{c}_2 \in \mathbb{R}^3$.

Constitutive Law of the LV

An active stress formulation was used to describe the LV's mechanical behavior in the cardiac cycle. In this formulation, the stress tensor $\boldsymbol{P}$ can be decomposed additively into a passive component $\boldsymbol{P}_{\text{p}}$ and an active component $\boldsymbol{P}_{\text{a}}$ (i.e., $\boldsymbol{P} = \boldsymbol{P}_{\text{a}} + \boldsymbol{P}_{\text{p}}$). The passive stress tensor was defined by $\boldsymbol{P}_{\text{p}} = dW/d\boldsymbol{F}$, where W is a strain energy function of a Fung-type transversely isotropic hyperelastic material [30] given by

$$W = \frac{1}{2}C\left(e^{Q-1}\right), \tag{11a}$$

where,

$$Q = b_{ff}E_{ff}^2 + b_{xx}\left(E_{ss}^2 + E_{nn}^2 + E_{sn}^2 + E_{ns}^2\right) + b_{fx}\left(E_{fn}^2 + E_{nf}^2 + E_{fs}^2 + E_{sf}^2\right). \tag{11b}$$

In Eq. (11), E_{ij} with $(i, j) \in (f, s, n)$ are components of the Green–Lagrange strain tensor $\boldsymbol{E}$ with f, s, n denoting the myocardial fiber, sheet, and sheet normal directions, respectively. Material parameters of the passive constitutive model are denoted by C, b_{ff}, b_{xx}, and b_{fx}.

The active stress $\boldsymbol{P}_{\text{a}}$ was calculated along the local fiber direction using a modified time varying elastance model,

$$\boldsymbol{P}_{\text{LV,a}} = T_{ref}\frac{Ca_0^2}{Ca_0^2 + ECa_{50}^2}C_t\mathbf{e}_f \otimes \mathbf{e}_{f_0} \tag{12}$$

In the above equation, $\mathbf{e}_f$ and $\mathbf{e}_{f_0}$ are, respectively, the local vectors defining the muscle fiber direction in the current and reference configuration, T_{ref} is the reference tension and Ca_0 denotes the peak intracellular calcium concentration. The length dependent calcium sensitivity ECa_{50} and the variable C_t are given by [29]

$$ECa_{50} = \frac{(Ca_0)_{max}}{\sqrt{\exp(B(l - l_0)) - 1}}, \tag{13}$$

$$C(t) = \begin{cases} \frac{1}{2}\left(1 - cos\left(\pi \frac{t}{t_0}\right)\right) & t < t_t \\ \frac{1}{2}\left(1 - cos\left(\pi \frac{t_t}{t_0}\right)\right) exp\left(\frac{t - t_t}{\tau}\right) & t \geq t_t \end{cases} \quad (14)$$

In Eq. (13), B is a constant, $(Ca_0)_{max}$ is the maximum peak intracellular calcium concentration and l_0 is the sarcomere length at which no active tension develops. In Eq. (14), t_0 is the time taken to reach the peak tension, t_t is the time at which isovolumic relaxation of LV starts and τ is the time constant of the isovolumic relaxation. Parameter values associated with the LV model are tabulated in Table 5.

Table 5

Fixed parameter values of the LV FE model

Parameter	Unit	Values
Exponent of strain energy function, b_{ff}	Unitless	29
Exponent of strain energy function, b_{xx}	Unitless	26.6
Exponent of strain energy function, b_{fx}	Unitless	13.3
Maximum peak intracellular Ca concentration, $(Ca_0)_{max}$	μM	4.35
Peak intracellular Ca concentration, Ca_0	μM	4.35
Parameter for isometric tension-sarcomere relationship, B	μm^{-1}	4.75
Sarcomere length at zero-active tension, l_0	μm	1.58
Time to peak tension, t_0	msec	275
Time to beginning of relaxation, t_t	msec	300

Parameters for each simulation cases are tabulated in Table 6.

Table 6

Parameters for simulation cases

	Passive stiffness C (Pa)	Active tension T_{ref} (kPa)	Distal arterial resistance, $R_{a,d}$ (kPa ms ml^{-1})	Resting venous volume V_{ven0} (ml)	Relaxation time constant τ (ms)
Normal	130	130	106	3370	25
G1	145	130	106	3100	50
G1-C1	145	91	106	3100	50
G1-C2	145	52	106	3100	50
G1-A1	145	130	212	3100	50
G1-A2	145	130	318	3100	50
G1-C-A	145	100	139.2	3100	50
G1-C-A-55	145	109	128	3100	50
G2	130	130	106	2950	50
G2-C1	130	100	106	2950	50
G2-C2	130	70	106	2950	50

	Passive stiffness C (Pa)	Active tension T_{ref} (kPa)	Distal arterial resistance, $R_{a,d}$ (kPa ms ml^{-1})	Resting venous volume V_{ven0} (ml)	Relaxation time constant τ (ms)
G2-A1	130	130	212	2950	50
G2-A2	130	130	318	2950	50
G2-C-55	130	91	106	2950	50
G2-C-50	130	91	106	2950	50

Abbreviations

DBP	Diastolic blood pressure
EF	Ejection fraction
EDV	End-diastolic volume
E_{ll}	Global longitudinal strain
E_{cc}	Global circumferential strain
HFpEF	Heart failure with preserved ejection fraction
HFrEF	Heart failure with reduced ejection fraction
HF	Heart failure
FE	Finite element
LV	Left ventricle
$R_{a,d}$	Peripheral resistance parameter
SBP	Systolic blood pressure
T_{ref}	Active tension parameter

References

1. Bhatia RS, Tu JV, Lee DS, et al. (2006). Outcome of heart failure with preserved ejection fraction in a population-based study. The New England Journal of Medicine, 355(3), 260–269. 10.1056/NEJMoa051530. [PubMed: 16855266]
2. Owan TE, Hodge DO, Herges RM, Jacobsen SJ, Roger VL, & Redfield MM (2006). Trends in prevalence and outcome of heart failure with preserved ejection fraction. The New England Journal of Medicine, 355(3), 251–259. 10.1056/NEJMoa052256. [PubMed: 16855265]
3. Borlaug BA, & Paulus WJ (2011). Heart failure with preserved ejection fraction: pathophysiology, diagnosis, and treatment. European Heart Journal, 32(6), 670–679. 10.1093/eurheartj/ehq426. [PubMed: 21138935]
4. Somaratne JB, Berry C, McMurray JJV, Poppe KK, Doughty RN, & Whalley GA (2009). The prognostic significance of heart failure with preserved left ventricular ejection fraction: a literature-based meta-analysis. European Journal of Heart Failure, 11(9), 855–862. 10.1093/eurjhf/hfp103. [PubMed: 19654140]

5. Tribouilloy C, Rusinaru D, Mahjoub H, et al. (2008). Prognosis of heart failure with preserved ejection fraction: a 5 year prospective population-based study. European Heart Journal, 29(3), 339–347. 10.1093/eurheartj/ehm554. [PubMed: 18156618]
6. Asif M, Egan J, Vasan S, et al. (2000). An advanced glycation endproduct cross-link breaker can reverse age-related increases in myocardial stiffness. Proceedings of the National Academy of Sciences. 10.1073/pnas.040558497.
7. Liu J, Masurekar MR, Vatner DE, et al. (2003). Glycation end-product cross-link breaker reduces collagen and improves cardiac function in aging diabetic heart. American Journal of Physiology. Heart and Circulatory Physiology 10.1152/ajpheart.00516.2003.
8. Solomon SD, Zile M, Pieske B, et al. (2012). The angiotensin receptor neprilysin inhibitor LCZ696 in heart failure with preserved ejection fraction: a phase 2 double-blind randomised controlled trial. Lancet. 10.1016/S0140-6736(12)61227-6.
9. Van Tassell BW, Arena R, Biondi-Zoccai G, et al. (2014). Effects of interleukin-1 blockade with anakinra on aerobic exercise capacity in patients with heart failure and preserved ejection fraction (from the D-HART Pilot Study). The American Journal of Cardiology. 10.1016/j.amjcard.2013.08.047.
10. Yamagami K, Oka T, Wang Q, et al. (2015). Pirfenidone exhibits cardioprotective effects by regulating myocardial fibrosis and vascular permeability in pressure overloaded hearts. American Journal of Physiology. Heart and Circulatory Physiology 10.1152/ajpheart.00137.2015.
11. Roh J, Houstis N, & Rosenzweig A (2017). Why don't we have proven treatments for HFpEF? Circulation Research, 120(8), 1243–1245. 10.1161/CIRCRESAHA.116.310119. [PubMed: 28408453]
12. Ponikowski P, Voors AA, Anker SD, et al. (2016). ESC Guidelines for the diagnosis and treatment of acute and chronic heart failure. European Heart Journal, 37(27), 2129–2200m. 10.1093/eurheartj/ehw128. [PubMed: 27206819]
13. Sengupta PP, & Marwick TH (2018). The many dimensions of diastolic function: a curse or a blessing? JACC: Cardiovascular Imaging. 10.1016/j.jcmg.2017.05.015.
14. Zile MR, Baicu CF, & Gaasch WH (2004). Diastolic heart failure—abnormalities in active relaxation and passive stiffness of the left ventricle. The New England Journal of Medicine, 350(19), 1953–1959. 10.1056/NEJMoa032566. [PubMed: 15128895]
15. Velagaleti RS, Gona P, Pencina MJ, et al. (2014). Left ventricular hypertrophy patterns and incidence of heart failure with preserved versus reduced ejection fraction. The American Journal of Cardiology, 113(1), 117–122. 10.1016/j.amjcard.2013.09.028. [PubMed: 24210333]
16. Zile MR, Gaasch WH, Carroll JD, et al. (2001). Heart failure with a normal ejection fraction: is measurement of diastolic function necessary to make the diagnosis of diastolic heart failure? Circulation, 104, 779–782. 10.1161/hc3201.094226. [PubMed: 11502702]
17. Kraigher-Krainer E, Shah AM, Gupta DK, et al. (2014). Impaired systolic function by strain imaging in heart failure with preserved ejection fraction. Journal of the American College of Cardiology, 63(5), 447–455. 10.1016/j.jacc.2013.09.052. [PubMed: 24184245]
18. Zou H, Xi C, Zhao X, et al. (2018). Quantification of biventricular strains in heart failure with preserved ejection fraction patient using hyperelastic warping method. Frontiers in Physiology, 9, 1295. 10.3389/fphys.2018.01295. [PubMed: 30283352]
19. Morris DA, Ma X-X, Belyavskiy E, et al. (2017). Left ventricular longitudinal systolic function analysed by 2D speckle-tracking echocardiography in heart failure with preserved ejection fraction: a meta-analysis. Open Hear, 4(2). 10.1136/openhrt-2017-000630.
20. Shah AM, Claggett B, Sweitzer NK, et al. (2015). Prognostic importance of changes in cardiac structure and function in heart failure with preserved ejection fraction and the impact of spironolactone. Circulation. Heart Failure 10.1161/CIRCHEARTFAILURE.115.002249.
21. Kawaguchi M, Hay I, Fetics B, & Kass DA (2003). Combined ventricular systolic and arterial stiffening in patients with heart failure and preserved ejection fraction: Implications for systolic and diastolic reserve limitations. Circulation, 107(5), 714–720. 10.1161/01.CIR.0000048123.22359.A0. [PubMed: 12578874]
22. Borlaug BA, Lam CSP, Roger VL, Rodeheffer RJ, & Redfield MM (2009). Contractility and ventricular systolic stiffening in hypertensive heart disease insights into the pathogenesis of heart

failure with preserved ejection fraction. Journal of the American College of Cardiology, 54(5), 410–418. 10.1016/j.jacc.2009.05.013. [PubMed: 19628115]

23. Dabiri Y, Sack KL, Shaul S, Sengupta PP, & Guccione JM (2018). Relationship of transmural variations in myofiber contractility to left ventricular ejection fraction: Implications for modeling heart failure phenotype with preserved ejection fraction. Frontiers in Physiology. 10.3389/fphys.2018.01003.
24. Genet M, Lee LC, Baillargeon B, Guccione JM, & Kuhl E (2016). Modeling pathologies of diastolic and systolic heart failure. Annals of Biomedical Engineering, 44(1), 112–127. 10.1007/s10439-015-1351-2. [PubMed: 26043672]
25. Adeniran I, MacIver DH, Hancox JC, & Zhang H (2015). Abnormal calcium homeostasis in heart failure with preserved ejection fraction is related to both reduced contractile function and incomplete relaxation: An electromechanically detailed biophysical modeling study. Frontiers in Physiology. 10.3389/fphys.2015.00078.
26. MacIver DH, & Townsend M (2008). A novel mechanism of heart failure with normal ejection fraction. Heart. 10.1136/hrt.2006.114082.
27. Shavik SM, Wall ST, Sundnes J, Burkhoff D, & Lee LC (2017). Organ-level validation of a cross-bridge cycling descriptor in a left ventricular finite element model: effects of ventricular loading on myocardial strains. Physics Reports, 5(21), e13392. 10.14814/phy2.13392.
28. Shavik S-M, Zhong L, Zhao X, & Lee LC (2019). In-silico assessment of the effects of right ventricular assist device on pulmonary arterial hypertension using an image based biventricular modeling framework. Mechanics Research Communications, 97, 101–111. [PubMed: 31983787]
29. Guccione JM, Waldman LK, & McCulloch AD (1993). Mechanics of active contraction in cardiac muscle : Part II—cylindrical models of the systolic left ventricle. Journal of Biomechanical Engineering, 115(February), 82–90. [PubMed: 8445902]
30. Guccione JM, Mcculloch AD, & Waldman LK (1991). Passive material properties of intact ventricular myocardium determined from a cylindrical model. Journal of Biomechanical Engineering, 113(1), 42–55. [PubMed: 2020175]
31. Logg A, Wells GN, & Mardel KA (2012). Automated solution of differential equations by the finite element method, 84. 10.1007/978-3-642-23099-8.
32. Maurer MS, King DL, El-Khoury Rumbarger L, Packer M, & Burkhoff D (2005). Left heart failure with a normal ejection fraction: Identification of different pathophysiologic mechanisms. Journal of Cardiac Failure, 11(3), 177–187. 10.1016/j.cardfail.2004.10.006. [PubMed: 15812744]
33. Shah AM (2013). Ventricular remodeling in heart failure with preserved ejection fraction. Current Heart Failure Reports, 10(4), 341–349. 10.1007/s11897-013-0166-4. [PubMed: 24097113]
34. Maurer MS, Burkhoff D, Fried LP, Gottdiener J, King DL, & Kitzman DW (2007). Ventricular structure and function in hypertensive participants with heart failure and a normal ejection fraction. The Cardiovascular Health Study. Journal of the American College of Cardiology. 10.1016/j.jacc.2006.10.061.
35. Prasad A, Hastings JL, Shibata S, et al. (2010). Characterization of static and dynamic left ventricular diastolic function in patients with heart failure with a preserved ejection fraction. Circulation. Heart Failure, 3(5), 617–626. 10.1161/CIRCHEARTFAILURE.109.867044. [PubMed: 20682947]
36. Zile MR, Baicu CF, Ikonomidis JS, et al. (2015). Myocardial stiffness in patients with heart failure and a preserved ejection fraction contributions of collagen and titin. Circulation. 10.1161/CIRCULATIONAHA.114.013215.
37. Shavik SM, Jiang Z, Baek S, & Lee LC (2018). High spatial resolution multi-organ finite element modeling of ventricular-arterial coupling. Frontiers in Physiology, 9(MAR). 10.3389/fphys.2018.00119.
38. Shavik SM, Tossas-Betancourt C, Figueroa CA, Baek S, & Lee LC (2020). Multiscale modeling framework of ventricular-arterial bi-directional interactions in the cardiopulmonary circulation. Frontiers in Physiology, 11, 2. 10.3389/fphys.2020.00002. [PubMed: 32116737]
39. Streeter DD, Spotnitz HM, Patel DP, Ross J, & Sonnenblick EH (1969). Fiber orientation in the canine left ventricle during diastole and systole. Circulation Research, 24(3), 339–347. 10.1161/01.RES.24.3.339. [PubMed: 5766515]

40. He K-L, Burkhoff D, Leng W-X, et al. (2009). Comparison of ventricular structure and function in Chinese patients with heart failure and ejection fractions >55% versus 40% to 55% versus. The American Journal of Cardiology, 103(6), 845–851. 10.1016/j.amjcard.2008.11.050. [PubMed: 19268743]
41. Mascherbauer J, Zotter-Tufaro C, Duca F, et al. (2017). Wedge pressure rather than left ventricular end-diastolic pressure predicts outcome in heart failure with preserved ejection fraction. JACC Hear Fail. 10.1016/j.jchf.2017.08.005.
42. Borlaug BA, Jaber WA, Ommen SR, Lam CSP, Redfield MM, & Nishimura RA (2011). Diastolic relaxation and compliance reserve during dynamic exercise in heart failure with preserved ejection fraction. Heart. 10.1136/hrt.2010.212787.
43. Lam CSP, Donal E, Kraigher-Krainer E, & Vasan RS (2011). Epidemiology and clinical course of heart failure with preserved ejection fraction. European Journal of Heart Failure, 13(1), 18–28. 10.1093/eurjhf/hfq121. [PubMed: 20685685]
44. Westermann D, Kasner M, Steendijk P, et al. (2008). Role of left ventricular stiffness in heart failure with normal ejection fraction. Circulation. 10.1161/CIRCULATIONAHA.107.716886.
45. Gorcsan J, & Tanaka H (2011). Echocardiographic assessment of myocardial strain. Journal of the American College of Cardiology, 58(14), 1401–1413. 10.1016/j.jacc.2011.06.038. [PubMed: 21939821]
46. Smiseth OA, Torp H, Opdahl A, Haugaa KH, & Urheim S (2015). Myocardial strain imaging: how useful is it in clinical decision making? European Heart Journal, 37(15), 1196–1207. 10.1093/eurheartj/ehv529. [PubMed: 26508168]
47. Hoit BD (2011). Strain and strain rate echocardiography and coronary artery disease. Circulation. Cardiovascular Imaging, 4(2), 179–190. 10.1161/CIRCIMAGING.110.959817. [PubMed: 21406664]
48. Butler J, Hamo CE, Udelson JE, et al. (2016). Exploring new endpoints for patients with heart failure with preserved ejection fraction. Circulation. Heart Failure 10.1161/CIRCHEARTFAILURE.116.003358.
49. Luo C, Ramachandran D, Ware DL, Ma TS, & Clark JW (2011). Modeling left ventricular diastolic dysfunction: classification and key indicators. Theoretical Biology & Medical Modelling. 10.1186/1742-4682-8-14.
50. Donaldson C, Palmer BM, Zile M, et al. (2012). Myosin cross-bridge dynamics in patients with hypertension and concentric left ventricular remodeling. Circulation. Heart Failure, 5(6), 803–811. 10.1161/CIRCHEARTFAILURE.112.968925. [PubMed: 23014131]
51. Borbély A, Van Der Velden J, Papp Z, et al. (2005). Cardiomyocyte stiffness in diastolic heart failure. Circulation, 111(6), 774–781. 10.1161/01.CIR.0000155257.33485.6D. [PubMed: 15699264]
52. Tanacli R, Hashemi D, Neye M, et al. (2020). Multilayer myocardial strain improves the diagnosis of heart failure with preserved ejection fraction. ESC Hear Fail. 10.1002/ehf2.12826.
53. Xu L, Pagano JJ, Haykowksy MJ, et al. (2020). Layer-specific strain in patients with heart failure using cardiovascular magnetic resonance: not all layers are the same. Journal of Cardiovascular Magnetic Resonance. 10.1186/s12968-020-00680-6.
54. Smith SP, Secomb TW, Hong BD, & Moulton MJ (2016). Time-dependent regional myocardial strains in patients with heart failure with a preserved ejection fraction. BioMed Research International. 10.1155/2016/8957307.
55. Gotschy A, Von Deuster C, Van Gorkum RJH, et al. (2019). Characterizing cardiac involvement in amyloidosis using cardiovascular magnetic resonance diffusion tensor imaging. Journal of Cardiovascular Magnetic Resonance. 10.1186/s12968-019-0563-2.
56. Pearlman ES, Weber KT, Janicki JS, Pietra GG, & Fishman AP (1982). Muscle fiber orientation and connective tissue content in the hypertrophied human heart. Laboratory Investigation.
57. Ennis DB, Nguyen TC, Riboh JC, et al. (2008). Myofiber angle distributions in the ovine left ventricle do not conform to computationally optimized predictions. Journal of Biomechanics. 10.1016/j.jbiomech.2008.08.007.
58. Triposkiadis F, Butler J, Abboud FM, et al. (2019). The continuous heart failure spectrum: Moving beyond an ejection fraction classification. European Heart Journal. 10.1093/eurheartj/ehz158.

59. Bers DM (2002). Cardiac excitation-contraction coupling. Nature. 10.1038/415198a.
60. Kelshiker M, Mayet J, Unsworth B, & Okonko D (2014). Basal septal hypertrophy. Current Cardiology Reviews. 10.2174/1573403X09666131202125424.
61. Weiss HR, Neubauer JA, Lipp JA, & Sinha AK (1978). Quantitative determination of regional oxygen consumption in the dog heart. Circulatory Shock, 42(3), 394–401. 10.1161/01.res.42.3.394.
62. Duncker DJ, Ishibashi Y, & Bache RJ (1998). Effect of treadmill exercise on transmural distribution of blood flow in hypertrophied left ventricle. American Journal of Physiology. Heart and Circulatory Physiology, 275(4 44–4), 1274–1282. 10.1152/ajpheart.1998.275.4.h1274.
63. Tan YT, Wenzelburger F, Lee E, et al. (2009). The pathophysiology of heart failure with normal ejection fraction. Exercise echocardiography reveals complex abnormalities of both systolic and diastolic ventricular function involving torsion, untwist, and longitudinal motion. Journal of the American College of Cardiology. 10.1016/j.jacc.2009.03.037.
64. Santos ABS, Roca GQ, Claggett B, et al. (2016). Prognostic relevance of left atrial dysfunction in heart failure with preserved ejection fraction. Circulation. Heart Failure 10.1161/CIRCHEARTFAILURE.115.002763.
65. Bianco CM, Farjo PD, Ghaffar YA, & Sengupta PP (2020). Myocardial mechanics in patients with normal LVEF and diastolic dysfunction. JACC: Cardiovascular Imaging. 10.1016/j.jcmg.2018.12.035.
66. Park JJ, Park JB, Park JH, & Cho GY (2018). Global longitudinal strain to predict mortality in patients with acute heart failure. Journal of the American College of Cardiology. 10.1016/j.jacc.2018.02.064.
67. Punnoose L, Burkhoff D, Rich S, & Horn EM (2012). Right ventricular assist device in end-stage pulmonary arterial hypertension: insights from a computational model of the cardiovascular system. Progress in Cardiovascular Diseases, 55(2), 234–243.e2. 10.1016/j.pcad.2012.07.008. [PubMed: 23009919]
68. Pezzuto S, & Ambrosi D (2014). Active contraction of the cardiac ventricle and distortion of the microstructural architecture. International Journal of Numerical Methods in Biomedical Engineering, 30(12), 1578–1596. 10.1002/cnm.2690.
69. Pezzuto S, Ambrosi D, & Quarteroni A (2014). An orthotropic active-strain model for the myocardium mechanics and its numerical approximation. European Journal of Mechanics - A/Solids, 48(1), 83–96. 10.1016/j.euromechsol.2014.03.006.

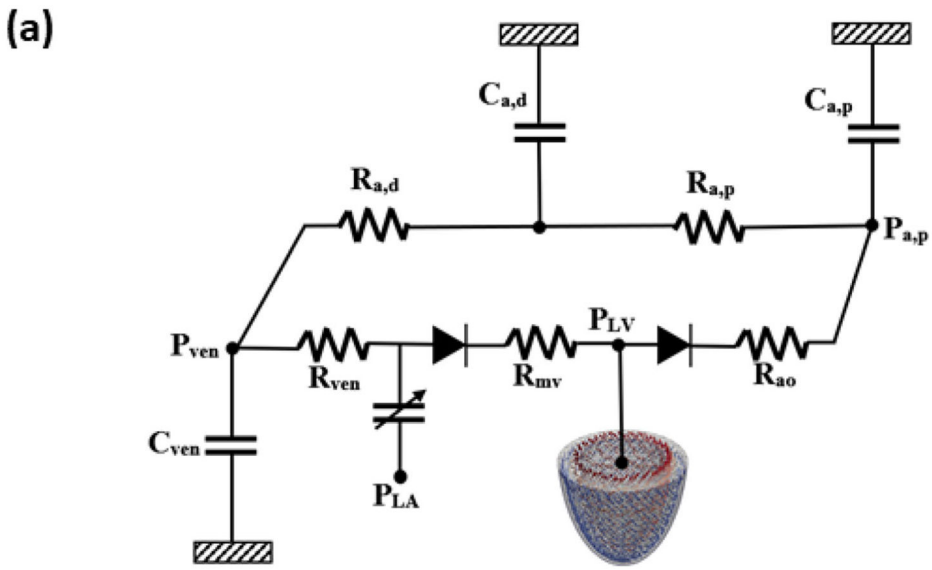

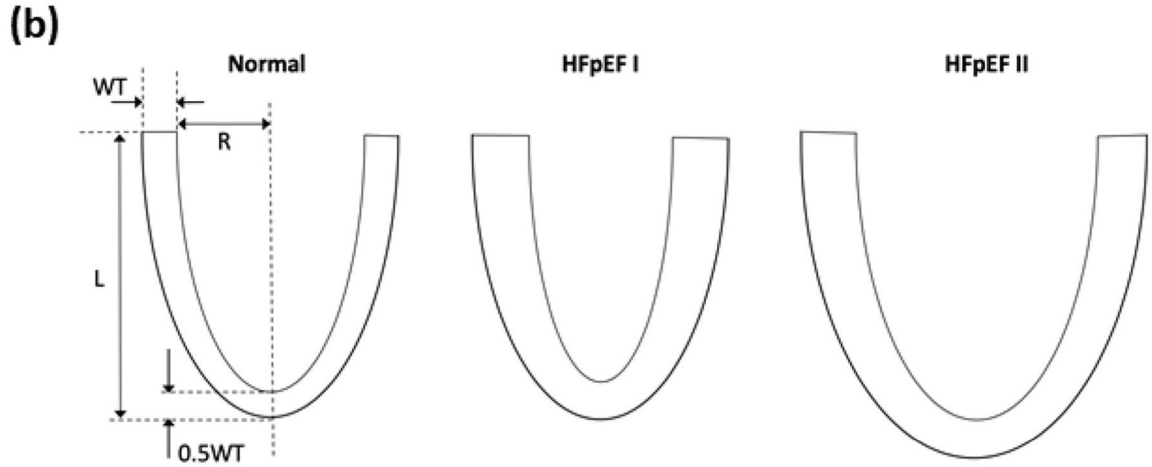

Geometrical dimensions and mass

	Normal	HFpEF I	HFpEF II
WT (cm)	1.13	1.38	1.45
R (cm)	2.00	1.82	2.00
L (cm)	8.30	8.10	8.85
Mass (g)	108.9	127.5	160.2

Fig. 1.

a Schematic of the computational framework showing the LV FE model coupled to a closed loop lumped parameter circulatory model. **b** LV geometries of *normal*, HFpEF I, and HFpEF II

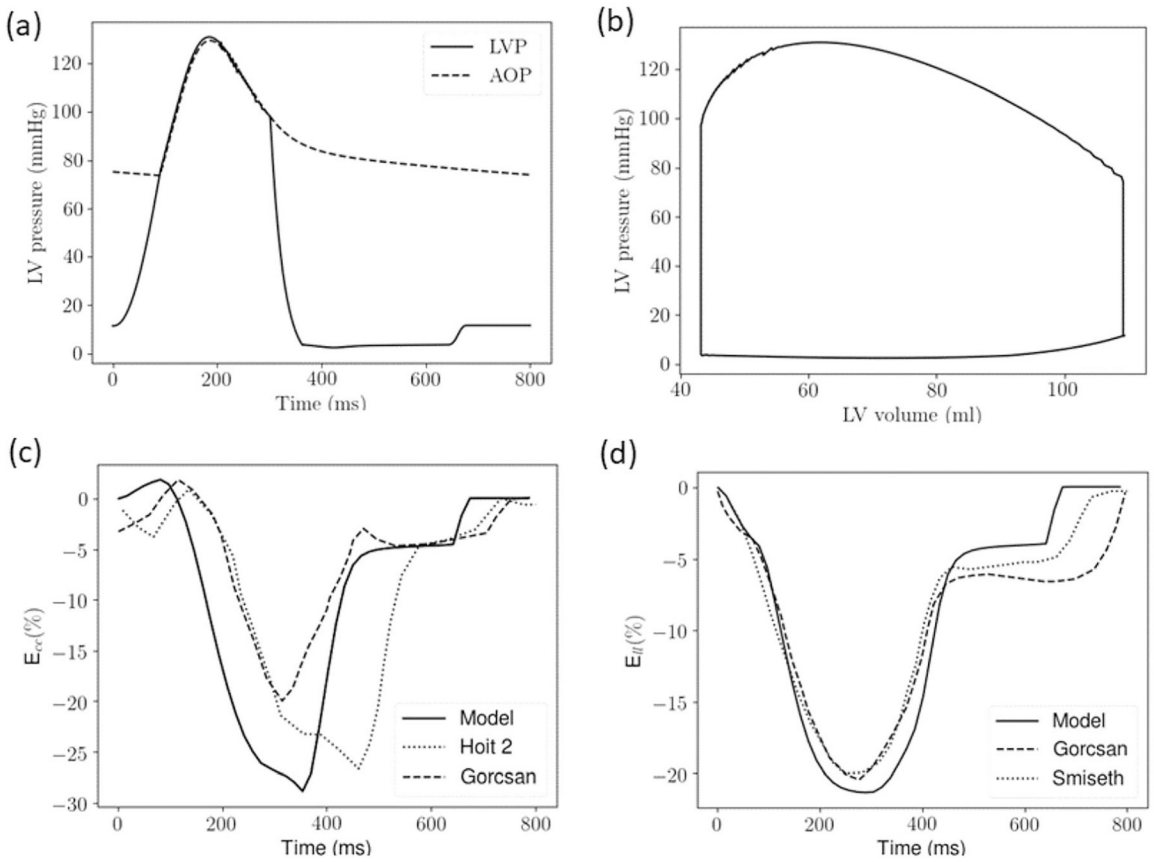

Fig. 2.

Normal case **a** Pressure waveforms of the LV (LVP) and proximal artery (AOP); **b** pressure–volume loop; **c** E_{cc} waveform compared with echo measurements (dotted [47] and dashed [45] lines); **d** E_{ll} waveform compared with echo measurements (dotted [46] and dashed [45] lines)

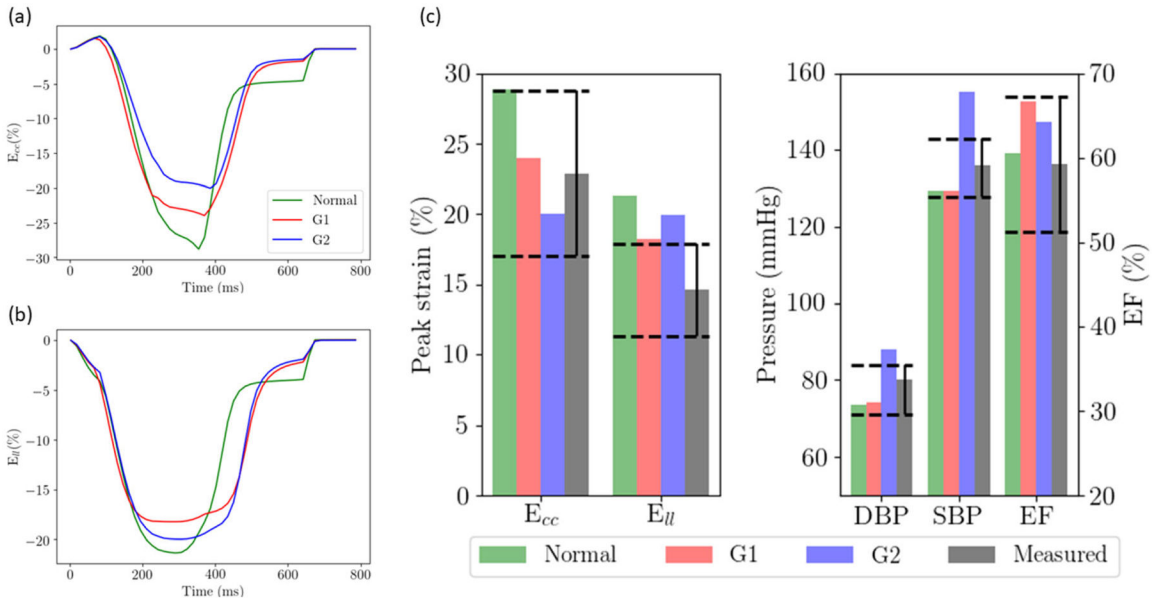

Fig. 3.

Effects of geometry, passive stiffness, and preload (case *G1* and *G2*) on **a** E_{cc} waveform; **b** E_{ll} waveform; **c** peak E_{cc}, E_{ll}, SBP, DBP, and EF with respect to values measured in HFpEF patients (black bars). Dashed lines show the range of the measured values in HFpEF patients

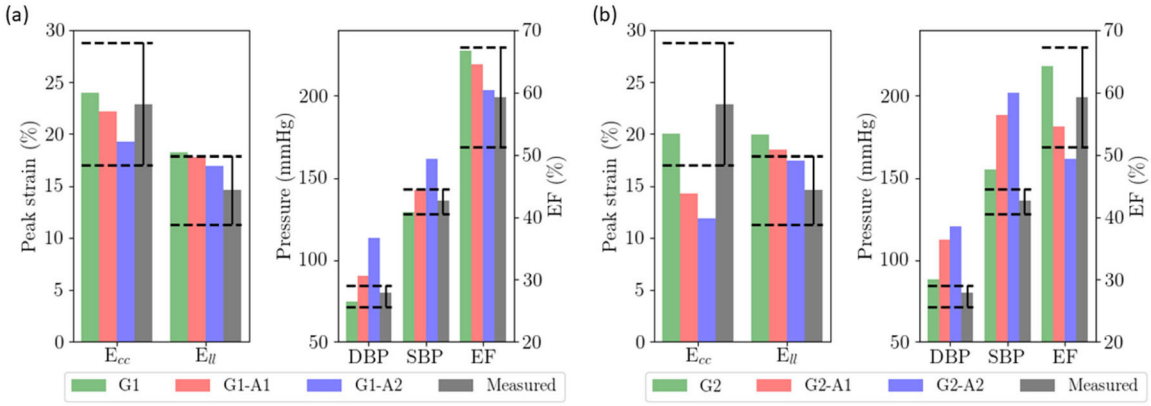

Fig. 4.

Effects of afterload on **a** HFpEF I geometry with a smaller LV cavity; **b** HFpEF II geometry with a dilated LV cavity. Dashed lines show the range of the measured values

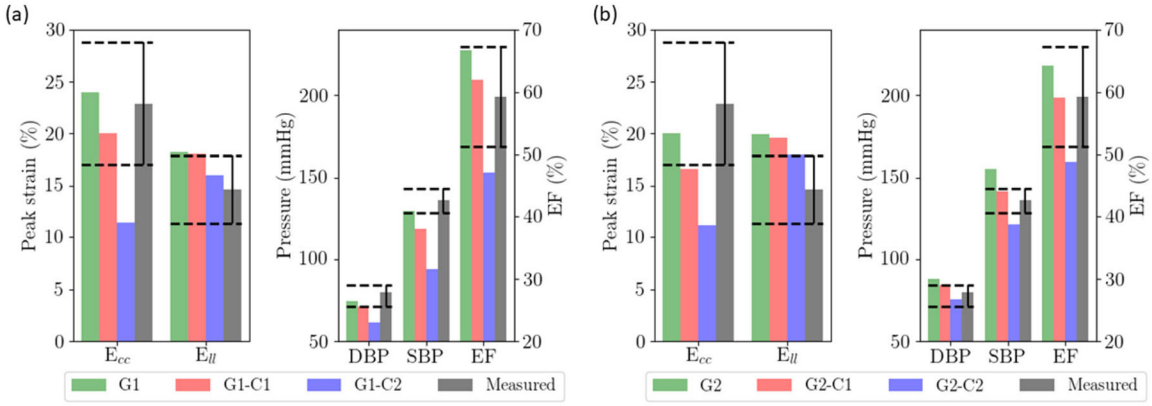

Fig. 5.

Effects of myocardial contractility on **a** HFpEF I geometry with a smaller LV cavity; **b** HFpEF II geometry with a dilated LV cavity. Dashed lines show the range of values measured in HFpEF patients

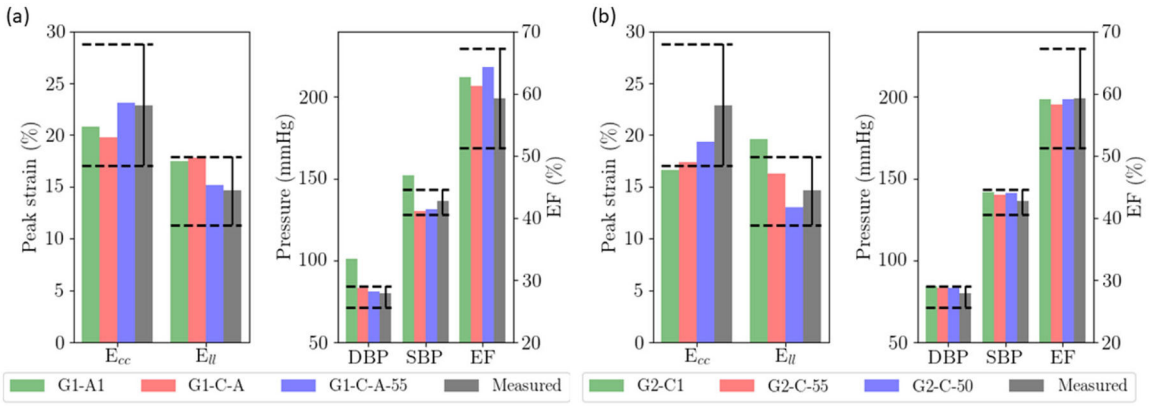

Fig. 6.

Combination of factors to reproduce clinical measurements. **a** HFpEF I geometry with a smaller LV cavity (*G1-A1* as starting reference); **b** HFpEF II geometry with a dilated LV cavity (*G2-C1* as starting reference). Dashed lines show the range of the measured values

Table 1

Simulation cases in this study

Geometry	Myocardial contractility	Vascular resistance	Passive myocardial stiffness	Case	Fiber angles (endo/epi)
Normal	Normal	Normal	Normal	Normal	60/−60°
HFpEF I	NC	NC	↑ 10%	*G1*	60/−60°
	↓ 30%	NC	↑ 10%	*G1-C1*	60/−60°
	↓ 60%	NC	↑ 10%	*G1-C2*	60/−60°
	NC	↑ 50%	↑ 10%	*G1-A1*	60/−60°
	NC	↑ 200%	↑ 10%	*G1-A2*	60/−60°
	↓ 23%	↑ 30%	↑ 10%	*G1-C-A*	60/−60°
	↓ 16%	↑ 20%	↑ 10%	*G1-C-A-55*	55/−55°
HFpEF - II	NC	NC	NC	*G2*	60/−60°
	↓ 23%	NC	NC	*G2-C1*	60/−60°
	↓ 46%	NC	NC	*G2-C2*	60/−60°
	NC	↑ 100%	NC	*G2-A1*	60/−60°
	NC	↑ 200%	NC	*G2-A2*	60/−60°
	↓ 30%	NC	NC	*G2-C-55*	55/−55°
	↓ 30%	NC	NC	*G2-C-50*	50/−50°

NC, no change with respect to normal

Table 2

Left ventricular geometry at end-diastole

Parameter	Normal		Case *G1*		Case *G2*	
	Model	Clinical [34]	Model	Clinical [44]	Model	Clinical [34]
Internal diameter (cm)	5.0	4.8±0.6	4.7	4.6 (4–5)	5.2	5.1±0.8
Wall thickness (cm)	0.8	0.8±0.1 *	1.02	1.12 (1.02–1.29) *	1.05	0.9±0.2 *

* Posterior wall thickness